International Journal of Hydrogen Energy 69 (2024) 1056–1068

Contents lists available at ScienceDirect

International Journal of Hydrogen Energy

journal homepage: www.elsevier.com/locate/he

Evaluation of hydrogen/ammonia substitute fuel mixtures for methane: Effect of differential diffusion

Xinyi Chen [a,*], Tobias Guivarch [b], Haris Lulic [a], Christian Hasse [a], Zheng Chen [c], Federica Ferraro [d], Arne Scholtissek [a]

[a] Institute for Simulation of Reactive Thermo-Fluid Systems, TU Darmstadt, Otto-Berndt-Straße 2, 64287, Darmstadt, Germany
[b] CentraleSupélec, Université Paris-Saclay, 3 Rue Joliot Curie, 91190 Gif-sur-Yvette, France
[c] SKLTCS, CAPT, College of Engineering, Peking University, Beijing, 100871, China
[d] Institute of Jet Propulsion and Turbomachinery, TU Braunschweig, Hermann-Blenk-Str. 37, 38108, Braunschweig, Germany

ARTICLE INFO

Handling Editor: Dr M Mahdi Najafpour

Keywords:
Ammonia
Hydrogen
Differential diffusion
Ignition
Stabilization mechanism

ABSTRACT

One strategy for utilizing ammonia as an energy vector is to replace conventional hydrocarbons with hydrogen-enriched ammonia in existing or retrofitted combustors. However, the strong differential diffusion effect of hydrogen can significantly alter the combustion properties and cause challenges in combustor operability. Therefore, this numerical study performs a systematic investigation on the effect of differential diffusion on fundamental combustion properties of ammonia/hydrogen fuel blends. The investigated combustion properties span from the initiation of combustion, i.e., ignition, to stretched flame propagation and ultimately to flame stabilization mechanisms. The objective is to evaluate the feasibility of hydrogen/ammonia/air mixtures as substitutes for methane/air particularly considering the implications of differential diffusion effects. To this end, four fuel blends with similar unstretched burning properties are selected: fuel lean ammonia/hydrogen (AH-L), fuel rich ammonia/hydrogen (AH-R), fuel lean methane (M-L) and fuel lean methane/hydrogen (MH-L). First, the forced ignition and stretched flame propagation are evaluated. It is found that the AH-L (AH-R) mixture has a large negative (positive) Markstein length, and thereby among the selected fuel blends, AH-L (AH-R) has the lowest (highest) minimum ignition energy. Then flame stabilization mechanisms are investigated. For a stable flame, AH-L (AH-R) has an intensified (weakened) flame base and a weak (strong) flame tip, which shows a higher flashback (blow-off) propensity. Based on the critical gradient theory, a novel stability regime diagram is proposed. With the regime diagram, the flame stabilization limits (central flashback, boundary layer flashback, stable, and blow-off) and flow conditions can be determined for burners of different sizes.

1. Introduction

The transition to a hydrogen economy is a promising pathway to significantly reduce greenhouse gas emissions while simultaneously satisfying the increasing energy demand [1]. However, challenges in hydrogen storage and transportation pose barriers for its implementation. Ammonia, also a carbon-free fuel, is gaining more attention due to its potential to serve as a hydrogen-carrying energy vector (with three atoms of hydrogen) [2]. High (volumetric) energy density, existing storage infrastructure and established transportation network, significantly lower storage requirements, and specific costs are all advantages of using ammonia as a unique energy storage medium. Furthermore, ammonia has very high hydrogen density and can be directly used as a fuel for power generation, such as in internal combustion engines and gas turbines [3]. Therefore, the direct utilization of ammonia can be considered a promising option for promoting the transition to a hydrogen-based economy.

The main challenges with ammonia combustion have been known for a very long time. The most important characteristics of ammonia combustion are [2,3]: high ignition energy, low burning velocity, narrow flammability range and slow chemical reaction. Given these characteristics, the use of pure ammonia, as low calorific-value fuel is usually not feasible in many applications. This makes flame enhancement important for the successful utilization of ammonia for power generation. An appealing strategy of fighting these challenges is doping ammonia with more reactive fuels. Hydrogen is preferred since the

---

* Corresponding author.
E-mail address: chen@stfs.tu-darmstadt.de (X. Chen).

https://doi.org/10.1016/j.ijhydene.2024.05.110
Received 20 March 2024; Received in revised form 1 May 2024; Accepted 8 May 2024
Available online 13 May 2024

ammonia/hydrogen blend can simultaneously achieve carbon-free combustion and flame enhancement. Besides, hydrogen can be easily produced via the catalytic decomposition of ammonia, and thereby no additional fuel storage is needed [4,5]. Ammonia/hydrogen blends can be tailored to a desired fuel reactivity by varying the ratio between hydrogen to ammonia. According to previous studies, laminar burning velocities of ammonia/hydrogen blends increase exponentially with hydrogen addition, especially at fuel rich conditions [2]. Similar burning rates to methane/air are measured for volumetric hydrogen fractions in the fuel between 0.4 and 0.5 [6,7]. Formally, these ammonia/hydrogen fuel blends satisfy some of the conditions for replacing conventional fuels, such as methane, in existing combustion hardware.

However, compared to conventional fuels, hydrogen is highly diffusive. Increasing hydrogen content in the fuel tends to increase the flame sensitivity to stretch [6]. The flame sensitivity to stretch is quantified by the Markstein length, where negative (positive) values cause unstable (stable) flame behavior. In a previous study, it was found that the Markstein length of ammonia/hydrogen blends decreases with hydrogen addition for fuel lean conditions, while it increases for fuel rich conditions [6]. For stoichiometric conditions, the Markstein length varies non-monotonically with hydrogen addition [7]. Therefore, the different transport properties of H_2 can introduce fundamental changes in combustion characteristics and present significant combustor design challenges. Recently, Goldmann et al. [4,5] conducted a series of experimental investigations on the boundary layer flashback for non-swirling premixed hydrogen/ammonia/air flames. They found that with a methane-like laminar burning velocity, the fuel lean NH_3/H_2 substitute mixtures show a higher flashback propensity. Similarly, Wiseman et al. [1] reported experimental measurements of the blow-out limits of premixed turbulent $NH_3/H_2/N_2$/air flame. It was revealed that the blow-out velocity of the fuel lean $NH_3/H_2/N_2$/air flames is an order of magnitude higher than that of methane/air flames characterized by nearly identical unstretched laminar flame properties. This finding was also supported by the Direct Numerical Simulations (DNS) results of temporally evolving turbulent premixed jet flames in their study. As for the pollution formation, Netzer et al. [8] conducted a two-dimensional DNS study and found that the spatial pattern of NO formation of $NH_3/H_2/N_2$/air flames is closely linked to the flame curvature and affected by thermal-diffusive effects of key species. These studies indicate that blending ammonia with hydrogen can enhance the flame but, at the same time, the differential diffusion effect of hydrogen can increase the risk of unwanted phenomena such as flashback and local NO formation. However, in these studies [1,4,5], the differential diffusion effect is always investigated e.g. in turbulent flames, it is still not clear how the differential diffusion and flame-stretch interaction fundamentally alter the combustion characteristics of ammonia/hydrogen blends.

This motivates the present study to focus on the effects of differential diffusion and stretch in a well-defined laminar configuration and investigate their individual influence on the fundamental combustion characteristics of hydrogen/ammonia/air flames. A systematic investigation is performed on combustion properties spanning from the initiation of combustion, i.e. the ignition characteristics, to stretched flame propagation and ultimately to the flame stabilization mechanisms. Furthermore, the combustion characteristics are compared between ammonia/hydrogen blends and methane related blends with similar unstretched flame characteristics. The objective is to evaluate the feasibility of hydrogen/ammonia/air mixture as a substitute for methane/air, with a primary focus on differential diffusion and stretch effects. The paper is structured as follows. First, the selected fuel blends, numerical setup and method are described in Section 2. Then, the simulation results are discussed in Section 3. In sub-section 3.1, an initial evaluation of unstretched flame structure and NO_x formation is first made for the selected fuel blends. The effect of differential diffusion on forced ignition and spherical flame propagation, and on Bunsen flame stabilization are investigated in sub-sections 3.2 and 3.3, respectively. Finally, the main conclusions are summarized in Section 4.

2. Numerical setup and method

For a sound comparison, a test matrix is constructed specifying NH_3/H_2 and CH_4/H_2 fuel blends with constant unstretched laminar burning velocity, as shown in Table 1. Given the extremely different reactivities of hydrogen and ammonia, the reactivity of the blend can be flexibly adjusted by varying the blending ratio of the NH_3/H_2, x_h, in the mixture:

$$x_h = \frac{X_{H_2}}{X_{H_2} + X_{NH_3}}, \tag{1}$$

where X_{H_2} and X_{NH_3} are the mole fractions of H_2 and NH_3, respectively. According to previous numerical and experimental studies [6,7,9], the laminar burning velocity of NH_3/H_2 blends approaches that of a CH_4/air flame when x_h is between 0.4 and 0.5. Besides, the adiabatic flame temperature T_{ad} and the thermal flame thickness l_T^0 of the NH_3/H_2 blends are also comparable to those of CH_4/air flames. The close match in unstretched laminar flame properties satisfies the utilization of NH_3/H_2 as a potential carbon-free surrogate fuel for methane. Based on a preliminary comparison of unstretched flame characteristics, an NH_3/H_2 fuel blend with $x_h = 0.45$ is selected. This blend demonstrates the highest similarity to methane in terms of burning velocity and overall power of the burner across the considered range of equivalence ratios. Two potential substitute mixtures: a fuel-lean (AH-L) and a fuel-rich NH_3/H_2 blend (AH-R) are chosen. In various applications, such as domestic boilers [10,11], methane/air flames are typically established with an equivalence ratio of around 0.85. Taking this as a reference, $\varphi = 0.85$ is also selected for the lean NH_3/H_2 case. The fuel-rich case with $\varphi = 1.35$ is analyzed keeping in mind the potential of two staged ammonia combustion for reduced NO_x and N_2O emissions [2]. Besides the CH_4/air reference mixture (M-L), a hydrogen enriched methane/air mixture (MH-L) with $x_h = 0.2$ (NH_3 replaced by CH_4 in Eqn. (1)) is also used for comparison. In this mixture, the blending ratio is close to the limit of hydrogen content for burner devices which were originally designed to operate with pure methane. For all the analyzed cases, the same unstretched laminar burning velocity of $s_L^0 = 0.3$ m/s is kept, as shown in Fig. 1.

The equivalence and blending ratio for the four different ammonia/hydrogen and methane/hydrogen fuel blends are summarized in Table 1, along with the important combustion properties and 1D laminar flame characteristics. In Table 1, T_{il} represents inner layer temperature, which is defined as a temperature at the location of peak heat release. $\mathrm{Le_{eff}}$ is the effective Lewis number. When fuel is composed of more than one species, the effective Lewis number is constructed out of the weighted Lewis numbers regarding the mass diffusivities of each fuel component in the mixture. In the literature, three weighting criteria were proposed: heat release rate based fraction, volume based fraction and diffusion based fraction [12]. In a recent study [13], it was found that the volume-based Lewis number is best suited for characterizing NH_3/H_2 mixtures. Therefore, a volume-based Lewis number is defined here:

$$\mathrm{Le_{eff}} = \sum X_i \mathrm{Le}_i, \tag{2}$$

where X_1 and X_2 are the volume fractions of both fuel components, and Le_1 and Le_2 their corresponding Lewis numbers. The laminar flame reference power, P_{spec}, is estimated based on fuel composition and lower heating value (LHV) per unit area of the burner, assuming a planar flame burning with its unstretched laminar burning velocity [14]:

$$P_{spec} = \sum \rho_i \mathrm{LHV}\, s_L^0, \tag{3}$$

where ρ_i is the density of fuel i and LHV is the lower heating value of the fuel blend (see Table 2). Note that the selected mixtures have comparable power that can be delivered from a planar flame. I_W represents the Wobbe index which is based on higher heating value (HHV) and specific gravity (G_S) [15,16]:

Table 1
Fundamental properties of selected fuel blends.

Case	x_h	φ	s_L^0 [m/s]	T_{ad} [K]	T_{il} [K]	l_T^0 [mm]	Le_{eff}	P_{spec} [kW/m^2]	I_W [MJ/m^3]
AH-L	0.45	0.85	0.3	2019.8	1679.9	0.567	0.806	754.6	23.26
AH-R	0.45	1.35	0.3	2010.6	1696.9	0.675	1.453	1061.9	23.26
M-L	0.00	0.85	0.3	2075.0	1634.8	0.490	0.966	801.2	48.84
MH-L	0.20	0.79	0.3	1998.9	1578.7	0.490	0.873	747.7	46.46

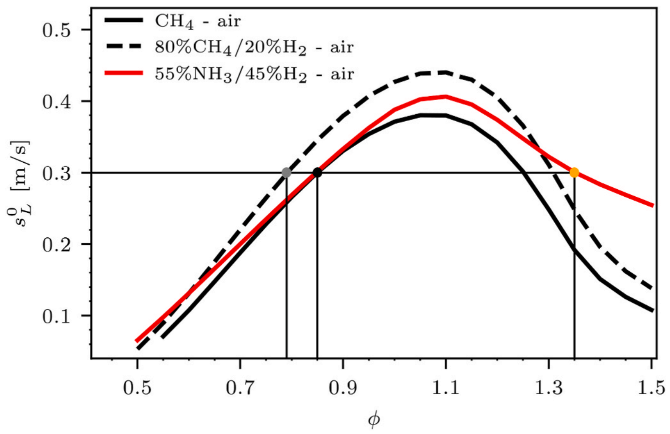

Fig. 1. Unstretched laminar burning velocity as a function of equivalence ratio for selected fuel blends.

Table 2
Lower and higher heating values of selected fuel blends.

Case	AH-L	AH-R	M-L	MH-L
LHV [MJ/Kg]	27.572	27.572	50.024	52.154
HHV [MJ/Kg]	33.033	33.033	55.510	58.138

$$I_W = \frac{\rho \text{HHV}}{\sqrt{G_S}}, \tag{4}$$

The Wobbe index indicates the potential interchangeability of different fuel gases entailing recalibration of operation parameters or significant modifications to the combustion equipment, which should be considered as a point when developing combustion systems for different blends. As shown in Table 1, the Wobbe index of the ammonia blends is very close to that of town gas ($I_W = 22.5 - 30.0$ MJ/m^3), while methane blends correspond to the usual range of natural gas ($I_W = 39.0 - 45.0$ MJ/m^3). This difference in the Wobbe index indicates significant retrofitting requirements for burners and/or its peripherals if the same power output is to be ensured in future combustors (not further discussed).

In the following analysis, important fundamental characteristics relevant to the combustion process will be evaluated and compared for the specified four fuel blends: the minimum ignition energy and Markstein length will be investigated in a one-dimensional (1D) forced ignition and spherical expanding flame configuration; and the flashback/blow-off limits will be investigated in a two-dimensional (2D) Bunsen flame configuration. These characteristics conceivably affect the fuel's performance inside combustion chambers, such as forced ignition, flame propagation and flame stabilization mechanisms in domestic burners, internal combustion engines and gas turbine combustors. The selected fuel blends will later be referred to by the abbreviations shown in Table 1 and i.e. AH-L and AH-R for the NH_3/H_2 lean and rich blend, respectively; M-L for pure CH_4 and MH-L for the CH_4/H_2 blend.

2.1. 1D forced ignition and spherical expanding flame configuration

A spherical expanding flame can be initiated from a central spark ignition in a quiescent mixture. During the ignition kernel evolution, the kernel is exposed to a positive stretch rate, which is inversely proportional to the flame radius. At the early propagation phase, the small ignition kernel is highly stretched and experiences strong combined effect of stretch and differential diffusion. This phenomenon is relevant to the initial combustion process, e.g. in practical engines.

The transient forced ignition and spherical flame propagation are simulated using the in-house code A-SURF [17,18], which solves the conservation equations for multi-component, reactive flows with the finite volume method. Detailed chemistry and transport are considered and the CHEMKIN packages [19] are utilized to calculate the detailed thermal-transport properties and reaction rates. A-SURF has been successfully used in previous studies on ignition and flame propagation [20–24]. Details of governing equations and numerical schemes are presented in Refs. [17,18], and thereby, are not repeated here.

As a result of the spherical symmetry, the simulations are conducted for a one-dimensional computational domain, with the radial coordinate varying between $0 \leq r \leq 30$ cm. The domain is initially filled with a static mixture at a temperature of $T_0 = 300$ K and pressure of $P_0 = 1$ atm. At both boundaries, $r = 0$ and 30 cm, zero flow velocities and zero gradients of mass fractions and temperature are enforced. For simplicity, the electrical energy discharge process (e.g. the plasma formation, shock wave) is not considered in the simulations. To mimic the real spark ignition process in experiments, the mixture is centrally ignited through energy deposition given by the following source term in the energy equation:

$$q_{ig}(r,t) = \begin{cases} \dfrac{E_{ig}}{\pi^{1.5} r_{ig}^3 \tau_{ig}} \exp\left[-\left(\dfrac{r}{r_{ig}} \right)^2 \right] & \text{if } t < \tau_{ig} \\ 0 & \text{if } t \geq \tau_{ig} \end{cases}, \tag{5}$$

where E_{ig} is the total input ignition energy, τ_{ig} the duration of energy deposition, and r_{ig} the radius of the energy deposited region. In simulations, the duration and radius of ignition energy deposition are fixed to be $\tau_{ig} = 0.4$ ms and $r_{ig} = 0.4$ mm, respectively. The minimum ignition energy (MIE) is obtained by a bisection method with an error below 2%.

2.2. 2D Bunsen flame configuration

A premixed Bunsen flame can be stabilized at the burner rim for a range of flow velocities. The flame surface is curved by the strained flow, showing a nearly conical structure. This configuration is suitable for the investigation of stretch effects due to the strong negative stretch rate at the flame tip and positive stretch rate at the flame base [23]. Upon closer inspection, the coupling of these effects with heat transfer to the burner rim results in a complex stabilization mechanism of the seemingly simple Bunsen flame. Considering the basic combustion properties of the fuel blends and a given set of operation parameters, it is therefore not always obvious whether the Bunsen flame does stabilize or will flashback/blow off.

Due to the axial symmetry of the configuration, the computational domain is modeled as a two-dimensional symmetrical rotational wedge. The geometrical parameters of the burner are shown in Fig. 2. At the

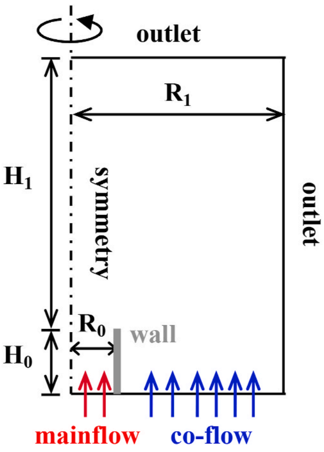

Fig. 2. Schematic of the two-dimensional computational domain. Dimensions are defined as: inlet tube height $H_0 = 15$ mm, domain height $H_1 = 67.5$ mm, inner radius of the inlet tube $R_0 = 6$ mm, tube wall thickness of 1 mm and overall domain radius $R_1 = 34$ mm.

inlet, a parabolic velocity profile is prescribed for the fuel/air main flow:

$$u(r) = u_0\left[1 - \left(\frac{r}{R_0}\right)^2\right], \tag{6}$$

where u_0 is the flow velocity at the tube centerline, and $R_0 = D/2$ is the inner radius of the inlet tube. Unless otherwise specified, the tube radius is $R_0 = 6$ mm. Minimizing the effect of the environment, a co-flow of pure nitrogen is prescribed with an inlet velocity of 0.1 m/s. Temperatures of the fresh mixture and co-flow are set to 300 K. Upstream, the main flow and co-flow are separated by a burner wall, which is modeled as an inert non-slip surface. The burner rim temperature is dependent on the thermal conductivity of the burner wall, which influences the flashback/blow-off propensity [25]. To account for the strong flame-burner interactions, conjugate heat transfer modeling is utilized in the present simulations. The solid burner wall is modeled as the property of steel with a thermal conductivity of $K = 30$ W/(m • K) due to its usage in domestic boilers [26]. This makes the burner wall temperature part of the solution, and it depends on the flame stabilization process. The top and side boundaries are treated as open outlets, where fixed atmospheric pressure is defined, and zero gradient boundary conditions are prescribed for all the other quantities. In simulations, the steady cold flow field is first obtained and then used as the initial velocity field for the subsequent reactive flow simulations.

A reactive flow solver based on OpenFOAM [27] is used for 2D direct numerical simulations with detailed chemistry and species transport. The finite volume method is used to solve the compressible conservation equations for multi-component reactive flows. Governing equations are given below:

$$\frac{\partial \rho}{\partial t} + \nabla \cdot (\rho \mathbf{v}) = 0, \tag{7}$$

$$\frac{\partial}{\partial t}(\rho \mathbf{v}) + \nabla \cdot (\rho \mathbf{v}\mathbf{v}) = -\nabla p + \nabla \cdot \boldsymbol{\tau}, \tag{8}$$

$$\frac{\partial}{\partial t}(\rho Y_k) + \nabla \cdot (\rho \mathbf{v} Y_k) = -\nabla \cdot \rho Y_k \mathbf{V}_k + \dot{\omega}_k \tag{9}$$

$$\rho \frac{D h_s}{D t} = \dot{\omega}_T + \nabla \cdot (\lambda \nabla T) - \nabla \cdot \left(\rho \sum_{k=1}^{N} h_{s,k} Y_k \mathbf{V}_k\right) \tag{10}$$

where ρ, $\mathbf{v}$, p, h_s, T, λ and $\boldsymbol{\tau}$ are the density, velocity, pressure, sensible enthalpy, temperature, thermal conductivity and viscous stress tensor of the mixture, respectively. In Eqn. (8), viscous stress tensor is computed using Stokes' law for Newtonian fluids. Y_k, $\dot{\omega}_k$ and $h_{s,k}$ are the mass fraction, net production rate, and sensible enthalpy corresponding to species k. $\mathbf{V}_k$ is the diffusion velocity vector of specie k, while $\dot{\omega}_T$ is the heat release by chemical reactions. In the simulations, the mixture-averaged model [28] with a correction velocity [29] is used to evaluate the mass diffusivities for all species and Cantera [30] is incorporated to obtain the transport coefficients. The reaction rates are calculated based on the DLB (dynamic load balancing) chemistry model [31]. The code has been validated in Refs. [32–34]. The computational grid consists of ~300k cells, with locally refined resolution in the flame region, resulting in the smallest cell size being 25 μm. This mesh resolution gives well resolved and grid independent results for the flame fronts. For each case, the simulation is run for at least three flow-through times after the flame is stabilized.

2.3. *Chemical kinetic model*

In the past decade, significant efforts have been devoted to understanding the complex chemical kinetics involved in ammonia combustion under various conditions [35]. Despite it, significant variations still persist in predicting the combustion characteristics across different kinetic models. The blending of different fuels with ammonia renders this task even more complex. In terms of the kinetics of the interaction between NH_3 and H_2 chemistry, most of the current kinetic mechanisms lack sufficient mechanistic coupling between the NH_3 and H_2 oxidation pathways. However, studies have shown that a very recent mechanism proposed by Stagni et al. [36] gives satisfactory results when compared to the experimental data, even in the case of ammonia/hydrogen blends with a high hydrogen content [37]. A validation of the mechanism with respect to comprehensive experimental data is available in Ref. [36] in terms of ignition delay time and laminar burning velocity. For methane relevant blends, a skeletal reaction mechanism is employed, which was developed for atmospheric methane/hydrogen/air combustion. The mechanism was obtained starting from the POLIMI kinetic mechanism using the reduction methodology described in Ref. [38] with the laminar burning velocity as the target property.

3. Results and discussion

3.1. *Unstretched flame structure and NO_x formation*

NO_x emissions are a critical problem throughout all stages of ammonia combustion. Therefore, in this sub-section, 1D freely propagating flame solutions are first obtained for all fuel blends to get an initial insight into the unstretched flame structures and NO_x formation. Calculations are carried out using the in-house Universal Laminar Flame (ULF) solver [39].

As shown in Fig. 3, a significantly high level of NO emissions can be observed in case AH-L (10417 ppm) compared to relatively moderate emissions for case AH-R (447 ppm). To quantify the contributions of different elementary reactions to the NO production/consumption, chemical pathway analysis is performed for cases AH-L and AH-R. As shown in Fig. 4, the HNO intermediate channel (i.e. R144) is the dominant NO production path in NH_3/H_2 blends for both cases. HNO is primarily produced by NH_i ($i = 0, 1, 2$) and converted to NO mainly through reactions with H and O [2]. In lean NH_3/H_2 flames, O/H radicals are abundant. Therefore, the NO formation path is favored. For rich conditions, the lower concentration of O/H radicals inhibits the conversion of NO from HNO, which explains the lower NO concentration in AH-R. Thus, for NH_3/H_2 flames, NO is generated mainly through the fuel NO pathway. In contrast, in the combustion of nitrogen-free fuels (i.e. M-L and MH-L), NO is mainly produced via the extended Zeldovich mechanism which is promoted by high temperatures ($T > 1800$ K) [40]. Therefore, with an adiabatic flame temperature of around 2000 K, only a small amount of NO is generated for M-L (44 ppm) and MH-L (23 ppm). In ammonia flames, however, due to the abundance of N, the Zeldovich

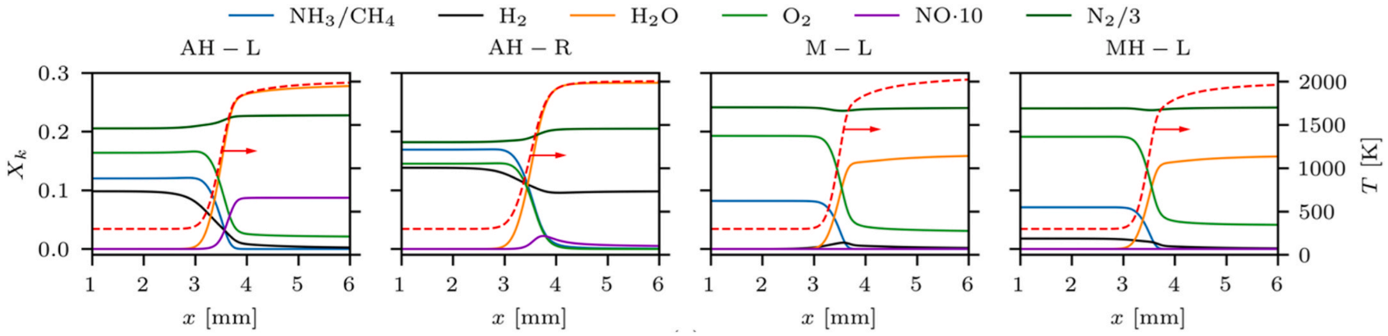

Fig. 3. Flame structures of one-dimensional unstretched flames for selected fuel blends.

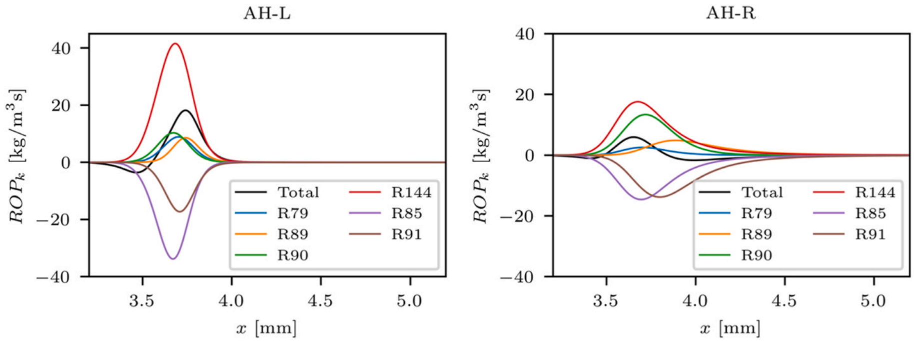

Fig. 4. NO production/consumption rates of dominant elementary reactions for AH-L and AH-R. R144: HNO + H = NO + H_2, R90: N + O_2 = NO + O, R89: N + OH = NO + H, R79: NH + O = NO + H, R85: NH + NO = N_2O + H, R91: N + NO = O + N_2.

mechanism is active even at low temperatures [2]. As shown in Fig. 4, the Zeldovich reaction R90: N + O_2 = NO + O is the second important NO formation route and R91: N + NO = O + N_2 has the second important contribution to the reduction of NO. Besides, R89: N+ OH = NO+ H also contributes to the production of NO. According to previous studies [41,42], the net influence of the Zeldovich mechanism on rich ammonia flames is a reduction of NO. This is the other reason responsible for the low NO concentration in AH-R.

With the increase of equivalence ratio, there is a trade-off in the relationship between NO and unburnt NH_3 emissions. As shown in Fig. 5, the total NO and NH_3 emissions both reach a minimum around φ = 1.35. This indicates that the use of a slightly rich condition (e.g., AH-R) can simultaneously reduce NO and NH_3. Furthermore, it is also noted that in the product of AH-R (see Fig. 3), the hydrogen concentration is relatively high, while the ammonia is completely consumed. Earlier studies also reported a non-zero mole fraction of hydrogen for fuel rich conditions for similar fuel blends and slightly lower equivalence ratios [43]. Rich conditions are relevant for two-stage combustors (as discussed for some gas turbine concepts) where the second combustion stage is employed to burn out the hydrogen residues.

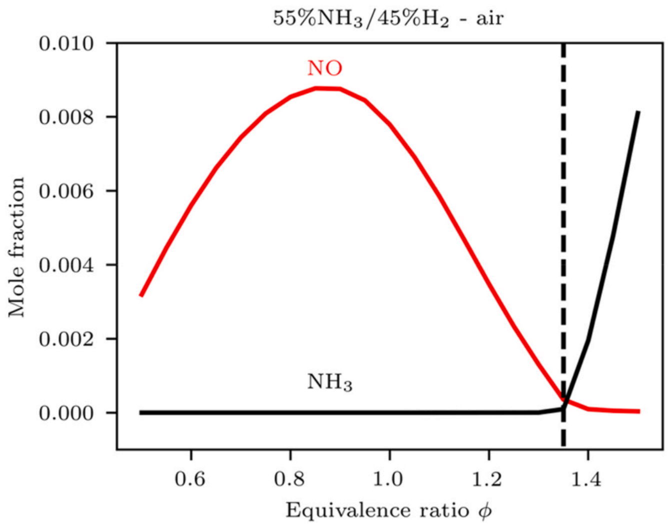

Fig. 5. NO and NH_3 emissions as a function of equivalence ratio for 55%NH_3/45%H_2 fuel blends.

3.2. Forced ignition and spherical flame propagation

In practical engines, combustion is usually initiated by a spark ignition. After ignition, a stretched flame kernel is propagating outwardly. To quantify the ignition characteristics, the minimum ignition energies (MIE) are calculated for different fuel blends. The results are summarized in Table 3. To visualize the stretched flame propagation, changes of the normalized flame propagation speed as a function of Karlovitz number for selected fuel blends are plotted in Fig. 6. In simulations, the flame radius, R_f , is defined as the location of local maximum heat release rate, and the flame propagation speed is obtained from numerical differentiation according to $U = \mathrm{d}R_f/\mathrm{dt}$. The flame propagation speed is normalized by U_0, which is the flame propagation speed at zero stretch rate. For outwardly propagating spherical flames, the overall stretch rate is $K = 2U/R_f$. The Karlovitz number is defined as

Table 3
Calculated minimum ignition energies and Markstein lengths for selected fuel blends.

Case	MIE (mJ)	L_b (mm)
AH-L	0.488	−0.938
AH-R	0.638	0.900
M-L	0.588	0.744
MH-L	0.563	0.262

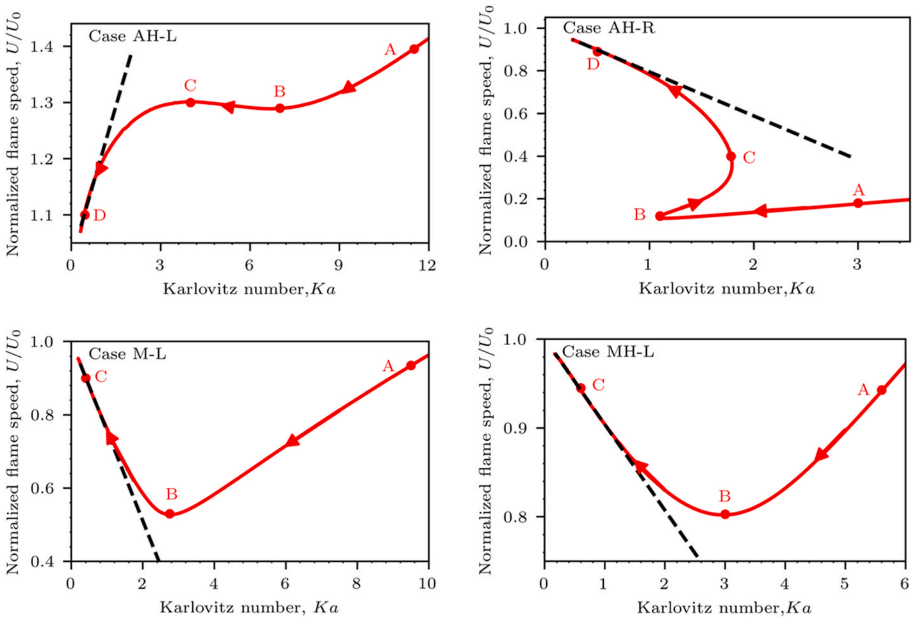

Fig. 6. Change of normalized flame speed as a function of Karlovitz number during the forced ignition process at the critical conditions for selected fuel blends.

Ka $= Kl_T^0/s_L^0$, where l_T^0 and s_L^0 are the flame thickness (defined based on maximum temperature gradient) and laminar flame speed of the one-dimensional unstretched planar flame, respectively.

As shown in Fig. 6, for the AH-L and the AH-R case, three distinct flame regimes are observed during the successful ignition process: the spark-assisted ignition kernel propagation regime (AB), the unsteady flame transition regime (BC), and the quasi-steady flame propagation regime (CD). In the spark-assisted ignition kernel propagation regime, the flame propagation strongly depends on the ignition energy. Therefore, the propagation speed of the ignition kernel decays quickly since the excess enthalpy from the ignition energy becomes dissipated and less influential at larger flame radii [20]. In the quasi-steady flame propagation regime, the flame propagation speed shows a linear correlation to the stretch rate, which implies constant Markstein length as the stretch rate approaches zero. Therefore, the Markstein length, L_b, and the unstretched flame propagation speed, U_0, the two most important global properties of a laminar flame subjected to aerodynamic stretching, can be predicted from the linear relationship: $U = U_0 - L_bK$ [44,45]. The calculated Markstein lengths are shown in Table 3, which quantifies the sensitivities of the flame response to stretch. It is interesting to observe that with the same amount of hydrogen addition, the fuel lean NH_3/H_2 blend shows a negative Markstein length, while the fuel rich blend shows a positive Markstein length. These results are consistent with the previous study on freely propagating spherical flames [6]. This implies that during the early phase of the forced ignition, the positive stretch rate imposed on the ignition kernel facilitates its propagation for AH-L, while it inhibits the ignition kernel evolution for AH-R. This explains why a higher MIE is required for successful ignition of the rich ammonia mixture of the AH-R case. Between the spark-assisted ignition kernel propagation regime and the quasi-steady flame propagation regime, there is an unsteady flame transition regime [20]. For the M-L and the MH-L case, only two distinct flame regimes are observed: the spark-assisted ignition kernel propagation regime (AB), and the quasi-steady flame propagation regime (BC). Both two cases show a positive Markstein length and the values of L_b are smaller than that of AH-R. Therefore, for mixtures with similar unstretched flame properties, the hydrocarbon mixtures of the M-L and the MH-L case are more difficult to ignite than the lean ammonia/hydrogen mixture of AH-L, but they are easier to ignite than the rich ammonia/hydrogen mixture of AH-R.

3.3. Bunsen flame stabilization

After ignition and flame propagation, the flame will be ultimately stabilized at the flame holder. In this sub-section, flame stabilization mechanisms are investigated in the 2D axisymmetric Bunsen flame configuration. First, the stable flame structures are compared for the four selected fuel blends. Then a fully Automated Flashback Detection (AutoFD) approach is introduced to investigate the flashback and blow-off limits.

3.3.1. Stable flame structure

Fig. 7 shows the contour plots of local heat release rate and radical concentrations for stable Bunsen flames of the considered fuel blends. The heat release rate is normalized with the maximum heat release rate of the unstretched 1D flame. For all cases, the same parabolic velocity profile with $u_0 = 1.2$ m/s is prescribed at the inlet, which is calculated from the unstretched burning velocity aiming for a half cone angle of 30 °. It is interesting to observe that, although all fuel blends have the same unstretched laminar burning velocity, the height and half-cone angle of the flames differ notably. In general, the flames of NH_3/H_2 blends (AH-L, AH-R) clearly show more severe nonuniformities of the heat release rate distribution along the flame flank compared to CH_4 and CH_4/H_2 blends (M-L, MH-L). In the AH-L case, the flame burns strongly at the flame base and weakens at the flame tip, which lowers the flame half-cone angle, increases flame height, and reduces the lift-off height. The flame in the AH-R case has a weak base and the highest lift-off height among all the investigated flames. It is burning intensely at the flame tip, which causes the highest half-cone angle and the lowest flame height for all cases.

For the AH-L case, local radical distribution is directly correlated to the local heat release rate. From the OH and H distribution at the flame tip, it can be concluded that the tip is close to opening. This is expected if the equivalence ratio of the inlet mixture is decreased or the hydrogen fraction is decreased [46–48]. For the AH-R case, OH and H radicals are concentrated around the flame tip and the concentration decreases moving towards the flame base. The OH radical concentration is significantly lower compared to the AH-L case, which is expected for these rich conditions where oxygen is deficient and directly affects OH concentration. The radical distribution for the cases M-L and MH-L is mostly uniform along the flame, with small non-uniformity notable for the MH-L case.

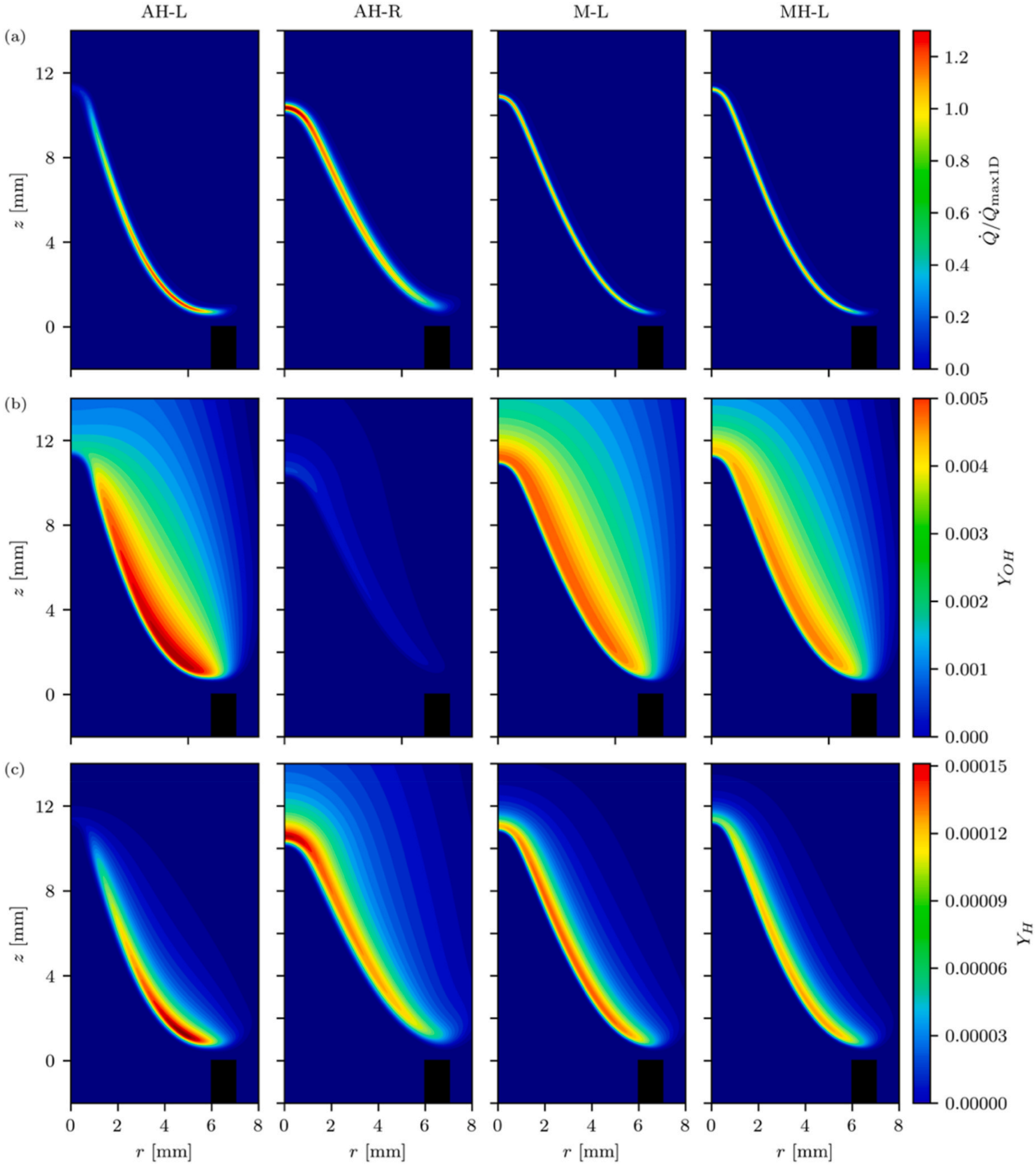

Fig. 7. Contour plots of (a) normalized heat release rate, (b) OH radical and (c) H radical for 2D stable Bunsen flames of the selected fuel blends.

In order to explain the different flame structures, the change of Karlovitz number, normalized heat release rate and normalized local equivalence ratio along the flame front are displayed in Fig. 8 for the selected fuel blends. The quantities are evaluated at the Y_{H_2O} isoline, the values of which are determined at the local heat release rate peak of the corresponding unstretched laminar planar flame, i.e. $Y_{H_2O} = 0.1662$ for AH-L, $Y_{H_2O} = 0.1853$ for AH-R, $Y_{H_2O} = 0.0902$ for M-L and $Y_{H_2O} = 0.0887$ for MH-L. Flame stretch, by definition, represents the time derivative of the logarithm of the surface area of an infinitesimal surface area element [49]:

$$K = \frac{1}{A}\frac{dA}{dt}, \tag{11}$$

After some transformation, stretch can be given in terms of stretch components [14]:

$$K = \nabla_t \cdot \mathbf{v} + s_d \kappa = K_s + K_c, \tag{12}$$

where the first term represents the aerodynamic strain rate imposed by the velocity field, and the second term is stretch due to curvature κ and flame propagation in the normal direction, which is given as a displacement velocity, s_d [14,50]. The stretch rate is usually given in a dimensionless form as Karlovitz number: $\mathrm{Ka} = K l_T^0 / s_L^0$. The local equivalence ratio is calculated based on Z_{Bilger} mixture fraction:

$$\varphi_{\mathrm{local}} = \frac{Z_{\mathrm{Bilger}}}{1 - Z_{\mathrm{Bilger}}} \cdot \frac{1 - Z_{st}}{Z_{st}}, \tag{13}$$

where $Z_{\mathrm{Bilger}} = (\beta - \beta_0)/(\beta_1 - \beta_0)$ is given in terms of coupling function β, with β_0 and β_1 being

Evaluated for oxidizer and fuel, respectively. Coupling function:

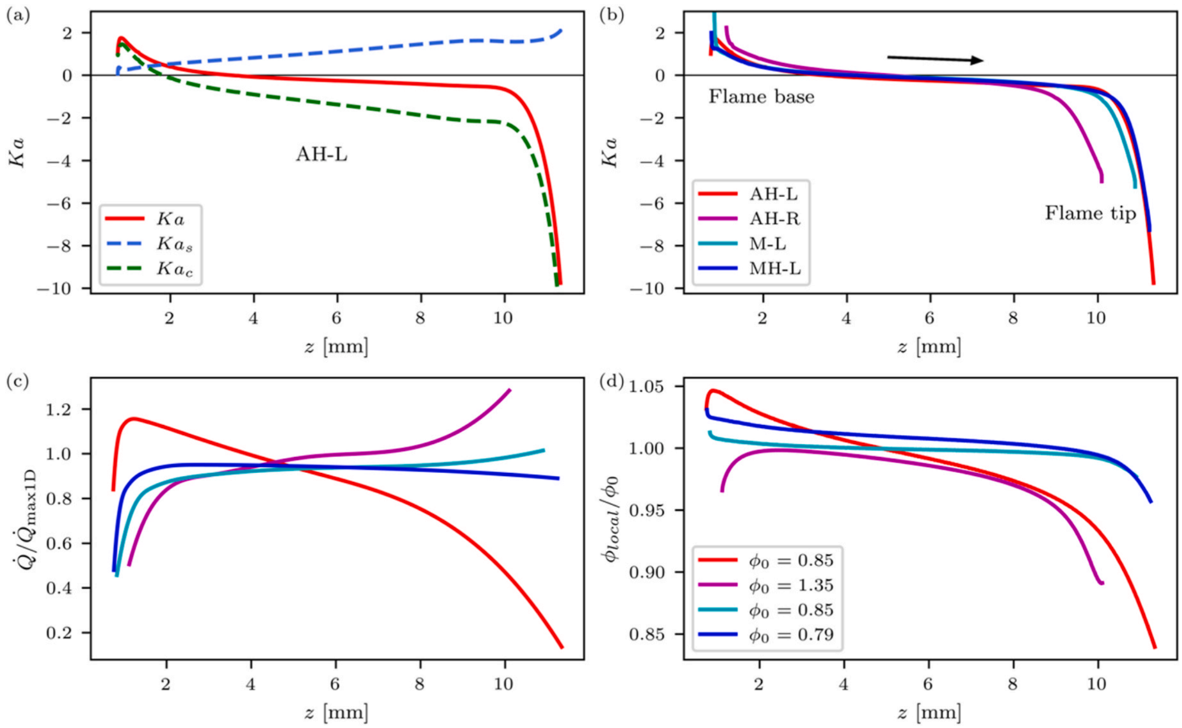

Fig. 8. Change of (a) dimensionless stretch, strain and curvature induced stretch as a function of z coordinate along the flame front for AH-L. Change of (b) Karlovitz number, (c) normalized heat release rate and (d) normalized local equivalence ratio as a function of z coordinate along the flame front for the four selected fuel blends.

$$\beta = \frac{2Z_C}{W_C} + \frac{Z_H}{2W_H} - \frac{Z_O}{W_O}, \tag{14}$$

is calculated using weights given in Ref. [51], where Z_C, Z_H and Z_O are elemental mass fractions of C, H and O, respectively. For ammonia/hydrogen blends, the first term on the RHS of Eqn. (14) is equal to zero.

As shown in Fig. 8(a), the flame base is positively stretched because of the contribution of positive strain. Moving towards the flame tip, negative curvature prevails over the positive strain and contributes increasingly until the flame tip, where the highest negative curvature is present. Similar trends of stretch components with quantitative differences are found throughout all cases and therefore are not shown here. Profiles of the total dimensionless stretch rate along the flame front are given in Fig. 8(b). As explained above, for all the cases, the flame exhibits a positive stretch starting at the flame base, decreasing to strongly negative at the flame tip, consistent with previous findings [23]. However, different trends are observed in heat release rate distribution for AH-R, AH-L, M-L, and MH-L, as shown in Fig. 8(c). For a burner stabilized Bunsen flame, the flame response to stretch can be attributed to a non-unity Lewis number of the deficient reactant, preferential diffusion effects and level of heat losses [14,49,52–54]. For the AH-L case, hydrogen is the reactant with the highest diffusivity and the deficient reactant with a Lewis number significantly lower than unity. Since the Bunsen flame is negatively stretched at the flame tip, a strong defocusing effect on the concentration of hydrogen at the flame tip is present. The concentration of hydrogen decreases at the flame front causing less stoichiometric mixture and weakened burning intensity (see Fig. 8(c) and d). This directly affects the spatial distribution of OH and H radicals, as well as the reaction rates of OH and H radicals. The concentration of ammonia, with a Lewis number close to unity, is not substantially affected by stretch [55]. For the AH-R case, the deficient reactant is oxygen with a Lewis number higher than unity. At the negatively stretched flame tip, heat is focused which increases the temperature, while the defocusing effect on hydrogen makes the mixture leaner (see Fig. 8(d)). This decrease in the equivalence ratio leads to a more stoichiometric mixture and strong burning intensity at the flame tip. At the flame base, a region of positive stretch is present for both cases (AH-L, AH-R). Positive stretch at the flame base contributes to strong burning intensity for the lean case, while the contribution for the rich case is adverse. Therefore, a high decrease (increase) in heat release rate is observed from flame base to tip for case AH-L (AH-R). For M-L and MH-L cases, the flame shows less sensitivity to the stretch rate. With a positive Markstein length, the flame tip is slightly enhanced for M-L, while it is slightly weakened for MH-L. This is because the fuel concentration of the mixture coming into the local flame cone is not uniform. Due to the radial diffusion of fuel, the mixture becomes leaner in the downstream direction. This scenario becomes more pronounced for MH-L with hydrogen addition since hydrogen is highly diffusive. When radial diffusion effect prevails the weak differential diffusion effect, weak burning intensity is observed at the flame tip for MH-L.

3.3.2. *A stability diagram considering fuel-specific flashback and blow-off limits*

In the Bunsen burner configuration, due to the non-slip conditions, the flow velocities are diminished near the burner walls. Flame burning velocities close to the walls also decrease due to the quenching of radicals and heat losses. In practical burners, flames are also simultaneously subjected to recirculation vortices, flame stretch and the effects of Lewis number [56]. These factors have the potential to substantially alter the flame anchoring process depending on the flow conditions, burner geometry and mixture properties. To maintain a robust flame anchoring at the burner rim, a kinematic balance must be achieved between local convective velocity and local burning velocity in the vicinity of the rim. In a premixed combustion system, the primary flashback mechanism of Bunsen flame is the boundary layer flashback (BLF). When the local convective velocity is lower than the local burning velocity near the burner wall, BLF occurs. On the contrary, when the local convective velocity is larger than the local burning velocity, blow-off occurs. Lewis and von Elbe [57] related the stabilization of flames at a cylindrical burner to two critical gradients of the gas velocity profile at the inner edge of the burner rim, i.e. g_B (blow-off limit) and g_F (flashback limit). For a flame to be stable, the condition $g_F < g < g_B$ must be satisfied.

To calculate the flashback and blow-off limits for the selected fuel blends, a fully Automated Flashback Detection approach is introduced: first, a stable flame is initiated at the burner rim at a high (low) velocity; by systematically decreasing (increasing) the inlet velocity, a flashback (blow-off) status can be detected and the flashback (blow-off) velocity is saved; then a bisection with stable velocity and flashback (blow-off) velocity is executed until the absolute tolerance has been reached. For a parabolic inlet velocity profile, the critical gradient at the burner rim is obtained as follows:

$$g_{F/B} = \left|\frac{\partial u_{F/B}}{\partial r}\bigg|_{r=R_0}\right| = \frac{2u_{0,F/B}}{R_0}, \tag{15}$$

where $u_{0,\mathrm{F/B}}$ is the onset flow velocity at the tube centerline for BLF/blow-off; and $R_0 = 6$ mm is the tube radius. For AH-R, a relatively larger tube with $R_0 = 7.5$ mm is used for the calculation of g_F. The AutoFD approach is developed and implemented into a Python code, which allows well-controlled and repeatable conditions for each run. In the Python program, the current state, i.e., flashback, blow-off or stable flame can be identified by processing the heat release rate profiles. A validation of the automatic numerical tool can be found in the Appendix. The calculated g_B and g_F for different fuel blends are summarized in Table 4. As previously discussed in Fig. 7, for the AH-L stable flame, the flame is enhanced at the flame base and is weakened close to the flame tip. This observation already indicates that this flame is anchoring more strongly to the wall and shows more resistance to the blow-off. However, with such intense reactivity at the base, the flame is more prone to BLF. As expected, among the four fuel blends, AH-L has the highest flashback limit of $g_F = 330$ 1/s and the highest blow-off limit of $g_B = 1845$ 1/s. On the contrary, the AH-R stable flame has a weak flame base. The BLF propensity decreases and the flame is more prone to blow-off. As shown in Table 4, AH-R shows the lowest flashback limit of $g_F = 172$ 1/s and the lowest blow-off limit of $g_B = 771$ 1/s. Both M-L and MH-L cases are less sensitive to the stretch rate and have moderate BLF and blow-off limits. Therefore, a trade-off between increased (decreased) flashback tendency and improved (declined) blow-off resistance is shown to be part of blending effects of fuel lean (rich) ammonia/hydrogen mixtures in premixed burners with analogous flame stabilization mechanisms.

In the previous study [58], it was found that g_B and g_F are both local variables, which are almost independent of the burner diameter. Therefore, the critical gradient theory can be applied to develop a stability diagram for variable burner diameters. Here, a more general velocity profile is prescribed at the inlet, where a constant velocity is assumed at the core of the flow and a parabolic profile is applied for the near-wall region (see Fig. 9):

$$u(r) = \begin{cases} u_0 \text{ for } r \le R_c \\ u_0\left(1 - \dfrac{(r-R_c)^2}{(R_0-R_c)^2}\right) \text{ for } R_c < r \le R_0 \end{cases}, \tag{16}$$

where u_0 is the flow velocity at the tube centerline, $R_0 = D/\ 2$ is the radius of the tube. Here, the tube radius R_0 is not fixed and could be any given value. The crossover radius is defined as $R_c = kR_0$ with k varying between 0 (parabolic velocity profile) and 1 (top hat velocity profile). From Eqn. (16), the gradient at the burner rim is obtained as:

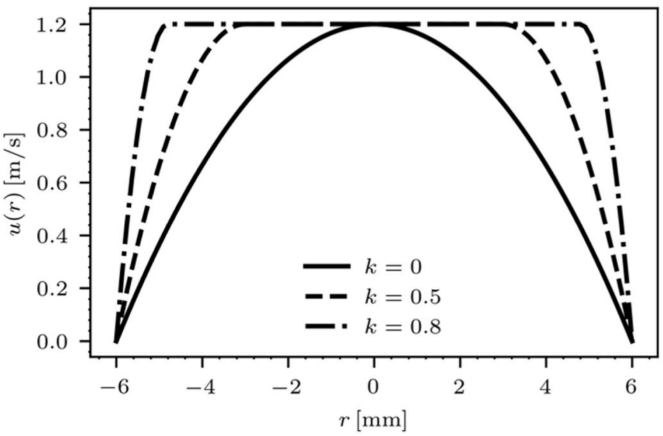

Fig. 9. Inlet velocity profiles with different k.

$$g = \left|\frac{\partial u}{\partial r}\bigg|_{r=R_0}\right| = \frac{2u_0}{R_0 - R_c}, \tag{17}$$

For a flame to be stable, the condition $g_F < g < g_B$ must be satisfied. Furthermore, the mean velocity of the flow is given by:

$$\bar{u} = \frac{\int_0^{R_0} 2\pi u(r) r dr}{\int_0^{R_0} 2\pi r dr} = u_0\left(1 + \frac{1}{6}\frac{R_c^4}{R_0^2(R_0-R_c)^2} - \frac{\frac{1}{2}R_0{}^2 - \frac{4}{3}R_0R_c + R_c^2}{(R_0-R_c)^2}\right), \tag{18}$$

which can be related to the flame shape via $\sin\alpha = s_L^0/\bar{u}$, where α is the half cone angle of the flame. From the above equations, an (α, D)-stability diagram is derived for $k = 0$, as shown in Fig. 10. The diagram shows the blow-off limit (dashed lines) and the flashback limit (solid lines) enclosing the stable flame region. Besides, a critical Reynolds number $\mathrm{Re}_c \approx 2300$ (red dashed lines) is presented to help to determine the flow conditions within the burner.

The stability diagram can hint at stabilizing measures or design changes if a flame tends to either blow-off or flashback. Fig. 11 displays different flame status of AH-R to give an intuitive flame information. With a gradual increase in inlet velocity (decrease in cone angle), the flame transitions from flashback to a stable state and eventually blow-off, depending on the competition between local convective velocity and burning velocity. Besides the primary boundary layer flashback, an additional trivial flashback mechanism, central flashback (i.e. Case A) is identified for small tube sizes. Central flashback occurs when the inlet velocity is lower than the local flame speed at the tube centerline. According to Eqn. (15), for a parabolic inlet velocity profile (i.e. $k = 0$), a critical tube diameter for central/boundary flashback phenomenon can be estimated as:

$$D_{c,flashback} = 2R_{c,flashback} = \frac{4u_{0,F}}{g_F} \approx \frac{4s_L^0}{g_F}, \tag{19}$$

For AH-R, the critical tube diameter is estimated as $D_{c,flashback} \approx 7$ mm. It should be noted that in Eqn. (19), the local flame speed at the tube centerline is estimated as the unstretched laminar burning velocity. When differential diffusion effect becomes important, i.e., when the flame tip of AH-R is intensified by the negative stretch rate, the local burning velocity is much larger than s_L^0 ($D_{c,flashback} > 7$ mm) at the tube centerline. Therefore, during the calculation, a larger tube diameter $D = 15$ mm is used in the AutoFD approach for AH-R. Below the critical tube diameter, the central flashback is the primary mechanism for the flashback of Bunsen flame. Above $D_{c,flashback}$, as the tube diameter increases, the flame stabilization cone angle range narrows. Furthermore, it is noted that the stable flame region can be shifted by the parameter k (inlet velocity profile in Fig. 9). For example, as shown in

Table 4
Calculated flashback and blow-off limits for selected fuel blends.

Case	g_F (1/s)	g_B (1/s)
AH-L	330	1845
AH-R	172	771
M-L	217	992
MH-L	230	1145

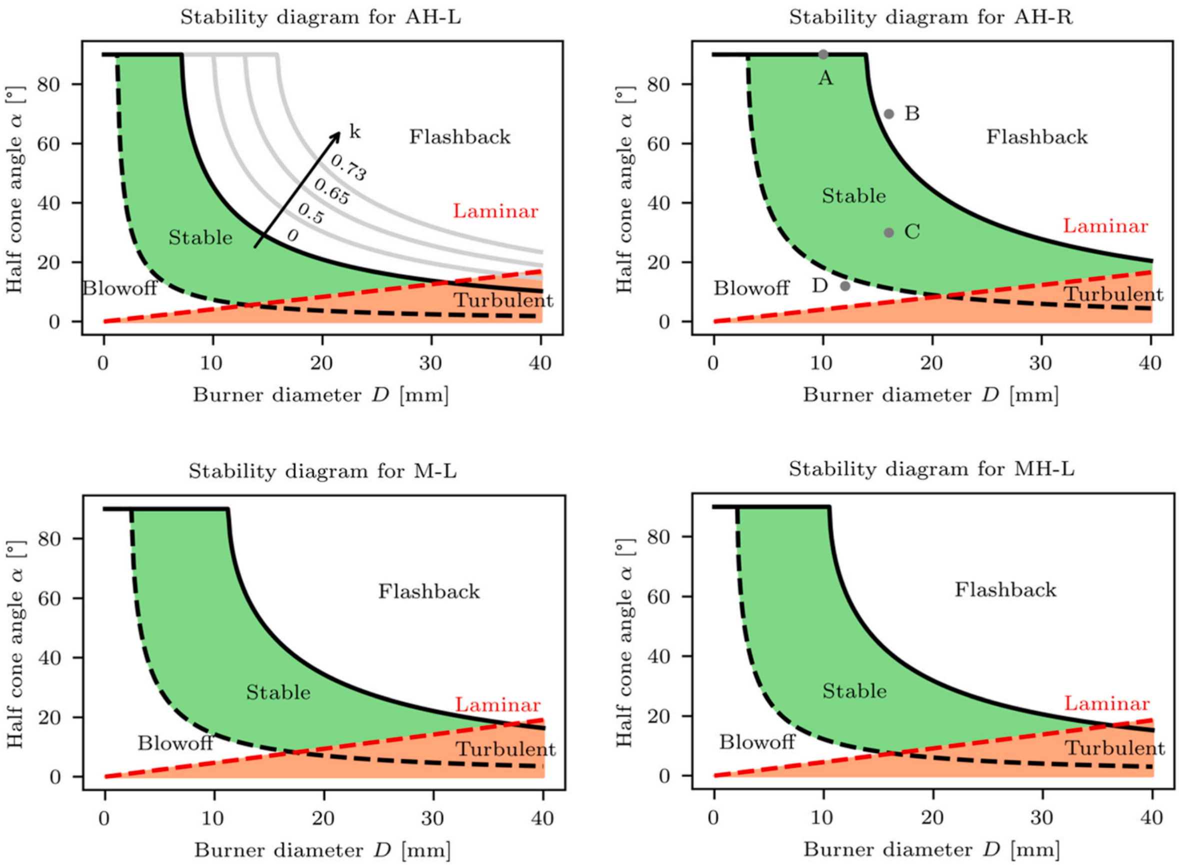

Fig. 10. Stability diagrams for selected fuel blends. $k = 0$, 0.5, 0.65, 0.73 for AH-L; $k = 0$ for AH-R, M-L and MH-L.

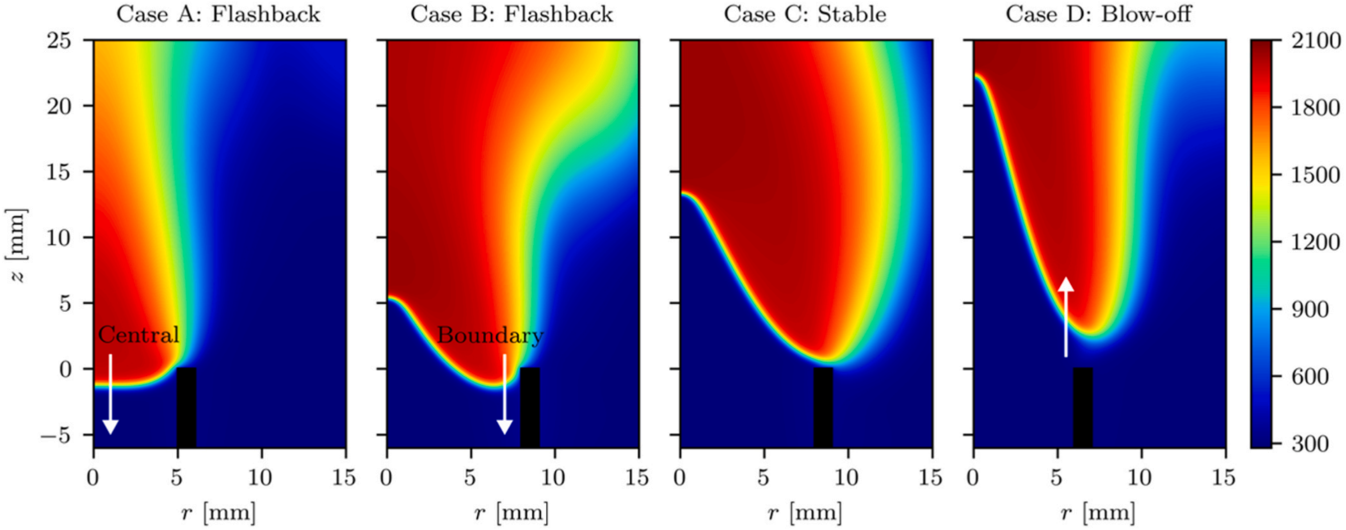

Fig. 11. Different flame status of AH-R. Case A: central flashback, $D = 12$ mm; Case B: boundary layer flashback, $D = 15$ mm; Case C: stable, $D = 15$ mm; Case D: blow-off, $D = 12$ mm. These cases correspond to points A-D marked in Fig. 9.

Fig. 10, a more top-hat like inlet velocity profile ($k > 0$) can shift the stable regime and prevent flashback for AH-L. In a preceding investigation, this metric has already been taken into account in the burner construction [32].

The stabilization regime diagram proposed in this study can serve as an orientation for adjusting the inflow boundary conditions and burner dimensions in future burner designs, such as domestic burners. However, it should be noted that in the present 2D numerical configuration, axisymmetry is assumed, similar to Ref. [26]. Therefore, only asymmetric flame propagation characteristics can be captured. In previous studies, a so-called polyhedral with flame front instabilities was observed for fuel lean NH_3/H_2 [5] and CH_4/H_2 blends [33,59] due to the presence of diffusional-thermal cellular instability. The cellular structure leads to a higher stretched burning velocity and is expected to further increase the BLF propensity for hydrogen-enriched but overall lean flames. The three-dimensional flame pattern necessitates additional investigation in future studies. Despite it, the current 2D configuration still allows for the elucidation of the underlying differential diffusion/stretch interactions behind flame stabilization mechanisms.

4. Conclusions and discussion

In this numerical study, four gaseous fuel blends with **similar unstretched laminar burning properties** are examined: lean CH_4 (M-L, $\varphi = 0.85$), lean CH_4/H_2 (MH-L, with 20 vol.-% H_2 and $\varphi = 0.79$), lean NH_3/H_2 (AH-L, with 45 vol.-% H_2 and $\varphi = 0.85$) and rich NH_3/H_2 (AH-R, with 45 vol.-% H_2 and $\varphi = 1.35$). The comparison of the combustion behavior of these fuel blends led to the following conclusions:

- **Lewis number and stretch effects:** the lean NH_3/H_2 flames clearly exhibit $Le < 1$ behavior with a negative Markstein length of $L_b =$ -0.938 mm, while rich NH_3/H_2 act oppositely ($Le > 1$ with a positive Markstein length of $L_b = 0.979$ mm). It is found that NH_3/H_2 flames show significantly higher sensitivity to stretch than the hydrocarbon reference cases (M-L and MH-L, $Le \sim 1$).
- **Minimum ignition energies:** lean NH_3/H_2 flames are easier to ignite (lower MIE) than the corresponding lean CH_4 and CH_4/H_2 flames. The rich NH_3/H_2 mixtures show the highest MIE among the investigated cases.
- **Flame stability:** lean NH_3/H_2 Bunsen flames have an intensified flame base, which shows the highest propensity to flashback, while rich NH_3/H_2 have a weak flame base, showing the highest propensity to blow-off. Compared to NH_3/H_2 flames, M-L and MH-L cases have moderate flashback and blow-off limits.

This study indicates that the strong flame stretch and differential diffusion effect of H_2 may bring significant challenges for combustor retrofitting. For example, the higher minimum ignition energy of fuel rich ammonia/hydrogen flame indicates potential misfire problems. Despite similar flame speeds, the significantly higher flashback limit of fuel lean ammonia/hydrogen flames and lower blow-off limit of fuel rich ammonia/hydrogen flames imply that these flames will stabilize differently, showing a different flame length, and likely exhibiting different flame dynamics. The higher flashback propensity of H_2-enriched ammonia is also relevant to control and safety. With these concerns, the stability regime diagram proposed in this study can serve as an orientation for adjusting the inflow boundary conditions and burner dimensions in future burner designs.

This study shows that, the unstretched laminar flame properties, conventionally used for flame characterization, are inadequate to explain such effects. These aspects have to be additionally taken into comprehensive consideration in the design also of more complex combustors, such as future engines and gas turbines.

CRediT authorship contribution statement

Xinyi Chen: Writing – original draft, Visualization, Methodology, Investigation, Conceptualization. **Tobias Guivarch:** Writing – review & editing, Visualization, Investigation. **Haris Lulic:** Writing – original draft, Visualization, Investigation. **Christian Hasse:** Writing – review & editing, Supervision, Project administration, Funding acquisition. **Zheng Chen:** Writing – review & editing, Software. **Federica Ferraro:** Writing – review & editing, Supervision, Methodology, Conceptualization. **Arne Scholtissek:** Writing – review & editing, Supervision, Project administration, Methodology, Funding acquisition, Conceptualization.

Declaration of competing interest

Acknowledgments

This work was funded by the Fritz and Margot Faudi-Foundation - Project No. 55200502. This work has been partly funded by the Deutsche Forschungsgemeinschaft (DFG, German Research Foundation) – project numbers 524004024 (AS) and 523792378 (CH) – SPP 2419.

Appendix. Validation of flashback limits and blow-off limits

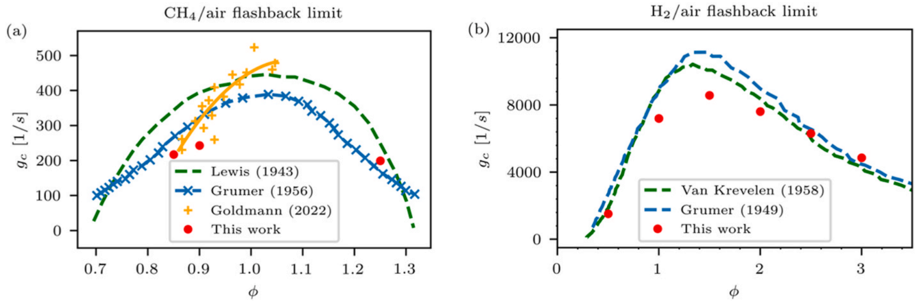

Fig. A1. Calculated flashback limits vs. experimental data for (a) methane/air and (b) hydrogen/air mixtures.

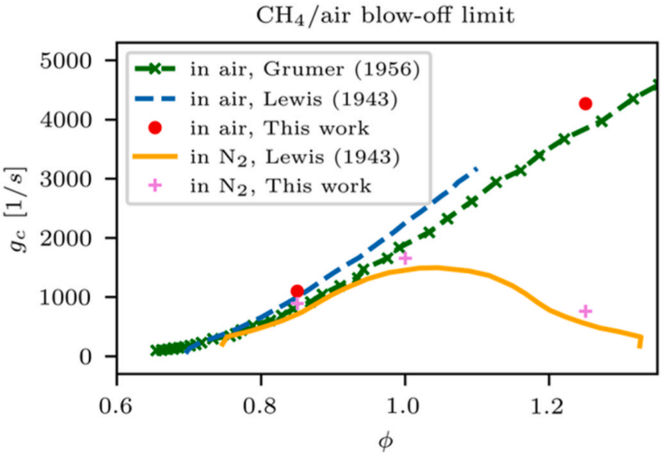

Fig. A2. Calculated blow-off limits vs. experimental data for methane/air mixture.

To calculate the flashback and blow-off limits, a fully Automated Flashback Detection (AutoFD) approach is developed and implemented into a Python code in this study, which allows well-controlled and repeatable conditions for each run. To validate the numerical simulation tool, our computational results are compared with experimental data obtained by Lewis et al. [57], Grumer et al. [60], Goldmann et al. [5] and Van Krevelen et al. [61]. Figure A1 shows that the computational results can reasonably predict the flashback limits for methane/air and hydrogen/air mixtures. The numerical and experimental results show the same trend: the flashback limit first increases and then decreases with the equivalence ratio, peaks at around $\varphi = 1.2$–1.5 for hydrogen/air mixture. Slight deviation is observed in the value of flashback limits, which can be explained due to the different or not specified burner material, burner geometry, heat transfer or quenching at the burner wall. As shown in Fig. A2, a better agreement is observed for the blow-off limits of the methane/air mixture. The computational results successfully predict the monotonic and non-monotonic trend of blow-off limits with the equivalence ratio in a co-flow of air and pure nitrogen, respectively. For the calculation of blow-off limits, the computational tool demonstrates a good predictive ability even for a quantitative comparison.

References

[1] Wiseman S, Rieth M, Gruber A, Dawson JR, Chen JH. A comparison of the blow-out behavior of turbulent premixed ammonia/hydrogen/nitrogen-air and methane–air flames. Proc Combust Inst 2021;38:2869–76.

[2] Kobayashi H, Hayakawa A, Somarathne KKA, Okafor EC. Science and technology of ammonia combustion. Proc Combust Inst 2019;37:109–33.

[3] Erdemir D, Dincer I. A perspective on the use of ammonia as a clean fuel: challenges and solutions. Int J Energy Res 2021;45:4827–34.

[4] Goldmann A, Dinkelacker F. Experimental investigation and modeling of boundary layer flashback for non-swirling premixed hydrogen/ammonia/air flames. Combust Flame 2021;226:362–79.

[5] Goldmann A, Dinkelacker F. Investigation of boundary layer flashback for non-swirling premixed hydrogen/ammonia/nitrogen/oxygen/air flames. Combust Flame 2022;238:111927.

[6] Lee J, Kim J, Park J, Kwon O. Studies on properties of laminar premixed hydrogen-added ammonia/air flames for hydrogen production. Int J Hydrogen Energy 2010; 35:1054–64.

[7] Ichikawa A, Hayakawa A, Kitagawa Y, Somarathne KKA, Kudo T, Kobayashi H. Laminar burning velocity and Markstein length of ammonia/hydrogen/air premixed flames at elevated pressures. Int J Hydrogen Energy 2015;40:9570–8.

[8] Netzer C, Ahmed A, Gruber A, Løvås T. Curvature effects on NO formation in wrinkled laminar ammonia/hydrogen/nitrogen-air premixed flames. Combust Flame 2021;232:111520.

[9] Li J, Huang H, Kobayashi N, He Z, Nagai Y. Study on using hydrogen and ammonia as fuels: combustion characteristics and NO$_x$ formation. Int J Energy Res 2014;38: 1214–23.

[10] Vriesde H, Mokhov AV, Levinsky HB. The impact of natural gas/hydrogen mixtures on the performance of end-use equipment: interchangeability analysis for domestic appliances. Appl Energy 2017;208:1007–19.

[11] Basso GL, Nastasi B, Garcia DA, Cumo F. How to handle the Hydrogen enriched Natural Gas blends in combustion efficiency measurement procedure of conventional and condensing boilers. Energy 2017;123:615–36.

[12] Bouvet N, Halter F, Chauveau C, Yoon Y. On the effective Lewis number formulations for lean hydrogen/hydrocarbon/air mixtures. Int J Hydrogen Energy 2013;38:5949–60.

[13] Gaucherand J, Laera D, Schulze-Netzer C, Poinsot T. Intrinsic instabilities of hydrogen and hydrogen/ammonia premixed flames: influence of equivalence ratio, fuel composition and pressure. Combust Flame 2023;256:112986.

[14] Poinsot T, Veynante D. Theoretical and numerical combustion: RT Edwards. 2005.

[15] Valera-Medina A, Pugh D, Marsh P, Bulat G, Bowen P. Preliminary study on lean premixed combustion of ammonia-hydrogen for swirling gas turbine combustors. Int J Hydrogen Energy 2017;42:24495–503.

[16] Valera-Medina A, Xiao H, Owen-Jones M, David WI, Bowen P. Ammonia for power. Prog Energy Combust Sci 2018;69:63–102.

[17] Chen Z, Burke MP, Ju Y. On the critical flame radius and minimum ignition energy for spherical flame initiation. Proc Combust Inst 2011;33:1219–26.

[18] Chen Z, Burke MP, Ju Y. Effects of Lewis number and ignition energy on the determination of laminar flame speed using propagating spherical flames. Proc Combust Inst 2009;32:1253–60.

[19] Kee RJ, Rupley FM, Meeks E, Miller JA. CHEMKIN-III: a FORTRAN chemical kinetics package for the analysis of gas-phase chemical and plasma kinetics. Sandia national lab. Livermore, CA (United States): SNL-CA); 1996.

[20] Chen X, Peng W, Gillard P, Courty L, Sankhe ML, Bernard S, et al. Effects of fuel decomposition and stratification on the forced ignition of a static flammable mixture. Combust Theor Model 2021;25:813–31.

[21] Chen X, Böttler H, Scholtissek A, Hasse C, Chen Z. Effects of stretch-chemistry interaction on chemical pathways for strained and curved hydrogen/air premixed flames. Combust Flame 2021;232:111532.

[22] Chen X, Zhao P, Dai P, Chen Z. On the prediction of hot spot induced ignition by the Livengood-Wu integral. Proc Combust Inst 2021;38:4709–16.

[23] Chen X, Wang Y, Zirwes T, Zhang F, Bockhorn H, Chen Z. Heat release rate markers for highly stretched premixed CH$_4$/air and CH$_4$/H$_2$/air flames. Energy Fuel 2021; 35:13349–59.

[24] Wang Y, Han W, Chen Z. Effects of fuel stratifcation on ignition kernel development and minimum ignition energy of n-decane/air mixtures. Proc Combust Inst 2019;37:1623–30.

[25] Bollinger LE, Edse R. Effect of burner-tip temperature on flash back of turbulent hydrogen-oxygen flames. Ind Eng Chem 1956;48:802–7.

[26] Vance FH, De Goey L, van Oijen JA. Development of a flashback correlation for burner-stabilized hydrogen-air premixed flames. Combust Flame 2022;243: 112045.

[27] Jasak H. OpenFOAM: open source CFD in research and industry. Int J Nav Archit Ocean Eng 2009;1:89–94.

[28] Hirschfelder JO, Curtiss CF, Bird RB. The molecular theory of gases and liquids. John Wiley & Sons; 1964.

[29] Coffee T, Heimerl J. Transport algorithms for premixed, laminar steady-state flames. Combust Flame 1981;43:273–89.

[30] Goodwin DGJCIoT. Cantera c++ user's guide, vol. 32; 2002.

[31] Tekgül B, Peltonen P, Kahila H, Kaario O, Vuorinen V. DLBFoam: an open-source dynamic load balancing model for fast reacting flow simulations in OpenFOAM. Comput Phys Commun 2021;267:108073.

[32] Luo Y, Ferraro F, Breicher A, Böttler H, Dreizler A, Geyer D, et al. A novel flamelet manifold parametrization approach for lean CH$_4$–H$_2$-air flames. Int J Hydrogen Energy 2023;48:407–21.

[33] Lulic H, Breicher A, Scholtissek A, Lapenna PE, Dreizler A, Creta F, et al. On polyhedral structures of lean methane/hydrogen Bunsen flames: combined experimental and numerical analysis. Proc Combust Inst 2023;39:1977–86.

[34] Steinhausen M, Ferraro F, Schneider M, Zentgraf F, Greifenstein M, Dreizler A, et al. Effect of flame retardants on side-wall quenching of partially premixed laminar flames. Proc Combust Inst 2023;39:3745–54.

[35] Alnasif A, Mashruk S, Shi H, Alnajideen M, Wang P, Pugh D, et al. Evolution of ammonia reaction mechanisms and modeling parameters: a review. Appl Energy Combust Sci 2023;15:100175.

[36] Stagni A, Cavallotti C, Arunthanayothin S, Song Y, Herbinet O, Battin-Leclerc F, et al. An experimental, theoretical and kinetic-modeling study of the gas-phase oxidation of ammonia. React Chem Eng 2020;5:696–711.

[37] Valera-Medina A, Amer-Hatem F, Azad A, Dedoussi I, De Joannon M, Fernandes R, et al. Review on ammonia as a potential fuel: from synthesis to economics. Energy Fuel 2021;35:6964–7029.

[38] Stagni A, Frassoldati A, Cuoci A, Faravelli T, Ranzi E. Skeletal mechanism reduction through species-targeted sensitivity analysis. Combust Flame 2016;163:382–93.

[39] Zschutschke A, Messig D, Scholtissek A, Hasse C. Universal laminar flame solver (ULF). Figshare Poster; 2017.

[40] Goto S, Furutani H, Koizumi K. Reduction of NO in reheat combustor of compound engine. Int Symp C0M0D1A 1990:645–9.

[41] Miller JA, Smooke MD, Green RM, Kee RJ. Kinetic modeling of the oxidation of ammonia in flames. Combust Sci Technol 1983;34:149–76.

[42] Shmakov A, Korobeinichev O, Rybitskaya I, Chernov A, Knyazkov D, Bolshova T, et al. Formation and consumption of NO in H_2+ O_2+ N_2 flames doped with NO or NH_3 at atmospheric pressure. Combust Flame 2010;157:556–65.

[43] Jiang Y, Gruber A, Seshadri K, Williams F. An updated short chemical-kinetic nitrogen mechanism for carbon-free combustion applications. Int J Energy Res 2020;44:795–810.

[44] Chen Z. On the extraction of laminar flame speed and Markstein length from outwardly propagating spherical flames. Combust Flame 2011;158:291–300.

[45] Chen Z. On the accuracy of laminar flame speeds measured from outwardly propagating spherical flames: methane/air at normal temperature and pressure. Combust Flame 2015;162:2442–53.

[46] Mizobuchi Y, Nambu T, Takeno T. Numerical study of tip opening of hydrogen/air Bunsen flame. Proc Combust Inst 2019;37:1775–81.

[47] Wang J, Wei Z, Yu S, Jin W, Xie Y, Zhang M, et al. Effects of stretch and preferential diffusion on tip opening of laminar premixed Bunsen flames of syngas/air mixtures. Fuel 2015;148:1–8.

[48] Mohammed AN, Jithin EV, Dineshkumar L, Ratna Kishore V, Mohammad A. Tip opening of burner-stabilized flames. Energy Fuel 2018;32:2344–54.

[49] Law C, Sung C. Structure, aerodynamics, and geometry of premixed flamelets. Prog Energy Combust Sci Technol 2000;26:459–505.

[50] Böttler H, Scholtissek A, Chen X, Chen Z, Hasse C. Premixed flames for arbitrary combinations of strain and curvature. Proc Combust Inst 2021;38:2031–9.

[51] Sutherland J, Smith P, Chen J. Quantification of differential diffusion in nonpremixed systems. Combust Theor Model 2005;9:365–83.

[52] Kumar P, Meyer TR. Experimental and modeling study of chemical-kinetics mechanisms for H_2–NH_3–air mixtures in laminar premixed jet flames. Fuel 2013;108:166–76.

[53] Bouvet N, Chauveau C, Gökalp I, Lee S-Y, Santoro RJ. Characterization of syngas laminar flames using the Bunsen burner configuration. Int J Hydrogen Energy 2011;36:992–1005.

[54] Fu J, Tang C, Jin W, Huang Z. Effect of preferential diffusion and flame stretch on flame structure and laminar burning velocity of syngas Bunsen flame using OH-PLIF. Int J Hydrogen Energy 2014;39:12187–93.

[55] Chen J, Fan W, Zhang H. Experimental and numerical study of curvature effects and NO formation in ammonia Bunsen flames. Fuel 2023;345:128207.

[56] Vance FH, Shoshin Y, de Goey L, van Oijen JA. Quantifying the impact of heat loss, stretch and preferential diffusion effects to the anchoring of bluff body stabilized premixed flames. Combust Flame 2022;237:111729.

[57] Lewis B, Von Elbe G. Stability and structure of burner flames. J Chem Phys 1943;11:75–97.

[58] Khitrin L, Moin P, Smirnov D, Shevchuk V. Peculiarities of laminar-and turbulent-flame flashbacks. Symposium (international) on combustion: Elsevier; 1965. p. 1285–91.

[59] Shi S, Breicher A, Trabold J, Hartl S, Barlow RS, Dreizler A, et al. Cellular structures of laminar lean premixed H_2/CH_4/air polyhedral flames. Appl Energy Combust Sci 2023;13:100105.

[60] Grumer J, Harris ME, Rowe VR. Fundamental flashback, blowoff, and yellow-tip limits of fuel gas-air mixtures. Pittsburgh, Pa.(USA): Bureau of Mines; 1955.

[61] Van Krevelen D, Chermin H. Generalized flame stability diagram for the prediction of interchangeability of gases. Symposium (International) on Combustion: Elsevier; 1958. p. 358–68.